Automatable sample fabrication process for pump-probe X-ray holographic imaging

Felix Büttner,[1,2,3,*] **Michael Schneider,**[1] **Christian M. Günther,**[1] **C. A. F. Vaz,**[2,4] **Bert Lägel,**[5] **Dirk Berger,**[6] **Sören Selve,**[6] **Mathias Kläui,**[2] **and Stefan Eisebitt**[1,7,8]

[1]*Institut für Optik und Atomare Physik, Technische Universität Berlin, Straße des 17. Juni 135, 10623 Berlin, Germany*
[2]*Institute of Physics, Johannes-Gutenberg-Universität Mainz, Staudinger Weg 7, 55128 Mainz, Germany*
[3]*Graduate School Materials Science in Mainz, Staudinger Weg 9, 55128 Mainz, Germany*
[4]*SwissFEL, Paul Scherrer Institut, 5232 Villigen PSI, Switzerland*
[5]*Nano Structuring Center, Technische Universität Kaiserslautern, Paul-Ehrlich-Str. 13, 67663 Kaiserslautern, Germany*
[6]*ZELMI, Technische Universität Berlin, Straße des 17. Juni 135, 10623 Berlin, Germany*
[7]*Helmholtz-Zentrum Berlin für Materialien und Energie GmbH, Hahn-Meitner-Platz 1, 14109 Berlin, Germany*
[8]*eisebitt@physik.tu-berlin.de*
[*]*felixbuettner@gmail.com*

Abstract:
Soft X-ray holography is a recently developed imaging technique with sub-50 nm spatial resolution. Key advantages of this technique are magnetic and elemental sensitivity, compatibility with imaging at free electron laser facilities, and immunity to *in-situ* sample excitations and sample drift, which enables the reliable detection of relative changes between two images with a precision of a few nanometers. In X-ray holography, the main part of the experimental setup is integrated in the sample, which consequently requires a large number of fabrication steps. Here we present a generic design and an automatable fabrication process for samples suitable, and optimized for, efficient high resolution X-ray holographic dynamic imaging. The high efficiency of the design facilitates the acquisition of magnetic images in a few minutes and makes fully automatic image reconstruction possible.

References and links

1. S. Eisebitt, J. Lüning, W. F. Schlotter, M. Lorgen, O. Hellwig, W. Eberhardt, and J. Stöhr, "Lensless imaging of magnetic nanostructures by X-ray spectro-holography," Nature **432**, 885–888 (2004).
2. T. Wang, D. Zhu, B. Wu, C. Graves, S. Schaffert, T. Rander, L. Müller, B. Vodungbo, C. Baumier, D. P. Bernstein, B. Bräuer, V. Cros, S. de Jong, R. Delaunay, A. Fognini, R. Kukreja, S. Lee, V. López-Flores, J. Mohanty, B. Pfau, H. Popescu, M. Sacchi, A. B. Sardinha, F. Sirotti, P. Zeitoun, M. Messerschmidt, J. J. Turner, W. F. Schlotter, O. Hellwig, R. Mattana, N. Jaouen, F. Fortuna, Y. Acremann, C. Gutt, H. A. Dürr, E. Beaurepaire, C. Boeglin, S. Eisebitt, G. Grübel, J. Lüning, J. Stöhr, and A. O. Scherz, "Femtosecond Single-Shot Imaging of Nanoscale

Ferromagnetic Order in Co/Pd Multilayers Using Resonant X-Ray Holography," Phys. Rev. Lett. **108**, 267403 (2012).

3. C. M. Günther, B. Pfau, R. Mitzner, B. Siemer, S. Roling, H. Zacharias, O. Kutz, I. Rudolph, D. Schondelmaier, R. Treusch, and S. Eisebitt, "Sequential femtosecond X-ray imaging," Nature Photon. **5**, 99–102 (2011).

4. E. Guehrs, C. M. Günther, B. Pfau, T. Rander, S. Schaffert, W. F. Schlotter, and S. Eisebitt, "Wavefield back-propagation in high-resolution X-ray holography with a movable field of view," Opt. Express **18**, 18922–18931 (2010).

5. J. Geilhufe, "Imaging 3 dimensional structures by Fourier transform holography," in preparation.

6. E. Guehrs, C. M. Günther, R. Könnike, B. Pfau, and S. Eisebitt, "Holographic soft X-ray omni-microscopy of biological specimens," Opt. Express **17**, 6710–6720 (2009).

7. F. Büttner, C. Moutafis, M. Schneider, B. Krüger, C. M. Günther, J. Geilhufe, C. v. Korff Schmising, J. Mohanty, B. Pfau, S. Schaffert, M. Foerster, T. Schulz, C. A. F. Vaz, J. H. Franken, H. J. M. Swagten, M. Kläui, and S. Eisebitt, "Topological mass of skyrmionic spin structures," submitted (2013).

8. T. Hauet, C. M. Günther, B. Pfau, M. E. Schabes, J.-U. Thiele, R. L. Rick, P. Fischer, S. Eisebitt, and O. Hellwig, "Direct observation of field and temperature induced domain replication in dipolar coupled perpendicular anisotropy films," Phys. Rev. B **77**, 184421 (2008).

9. D. Stickler, R. Frömter, H. Stillrich, C. Menk, C. Tieg, S. Streit-Nierobisch, M. Sprung, C. Gutt, L.-M. Stadler, O. Leupold, G. Grübel, and H. P. Oepen, "Soft X-ray holographic microscopy," Appl. Phys. Lett. **96**, 042501 (2010).

10. W. F. Schlotter, J. Lüning, R. Rick, K. Chen, A. Scherz, S. Eisebitt, C. M. Günther, W. Eberhardt, O. Hellwig, and J. Stöhr, "Extended field of view soft x-ray Fourier transform holography: toward imaging ultrafast evolution in a single shot," Opt. Lett. **32**, 3110–3112 (2007).

11. B. Pfau, C. M. Günther, S. Schaffert, R. Mitzner, B. Siemer, S. Roling, H. Zacharias, O. Kutz, I. Rudolph, R. Treusch, and S. Eisebitt, "Femtosecond pulse x-ray imaging with a large field of view," New J. Phys. **12**, 095006 (2010).

12. B. Pfau, C. M. Günther, E. Guehrs, T. Hauet, H. Yang, L. Vinh, X. Xu, D. Yaney, R. Rick, S. Eisebitt, and O. Hellwig, "Origin of magnetic switching field distribution in bit patterned media based on pre-patterned substrates," Appl. Phys. Lett. **99**, 062502 (2011).

13. C. M. Günther, O. Hellwig, A. Menzel, B. Pfau, F. Radu, D. Makarov, M. Albrecht, A. Goncharov, T. Schrefl, W. F. Schlotter, R. Rick, J. Lüning, and S. Eisebitt, "Microscopic reversal behavior of magnetically capped nanospheres," Phys. Rev. B **81**, 064411 (2010).

14. G. Schütz, W. Wagner, W. Wilhelm, P. Kienle, R. Zeller, R. Frahm, and G. Materlik, "Absorption of circularly polarized x rays in iron," Phys. Rev. Lett. **58**, 737–740 (1987).

15. http://www.silson.com/

16. K. Suzuki, J. Matsui, and T. Torikai, "SiN membrane masks for x-ray lithography," J. Vac. Sci. Technol. **20**, 191–194 (1982).

17. http://www.sdk.co.jp/

18. S. Yasin, D. Hasko, and H. Ahmed, "Comparison of MIBK/IPA and water/IPA as PMMA developers for electron beam nanolithography," Microelectron. Eng. **61–62**, 745–753 (2002).

19. B. Enders, K. Giewekemeyer, T. Kurz, S. Podorov, T. Salditt, "Non-iterative coherent diffractive imaging using a phase-shifting reference frame," New J. Phys. **11**, 043021 (2009).

20. W. F. Schlotter, "Lensless Fourier Transform Holography with Soft X-Rays," Dissertation, Stanford University (2007).

21. F. Büttner, C. Moutafis, A. Bisig, P. Wohlhüter, C. M. Günther, J. Mohanty, J. Geilhufe, M. Schneider, C. v. Korff Schmising, S. Schaffert, B. Pfau, M. Hantschmann, M. Riemeier, M. Emmel, S. Finizio, G. Jakob, M. Weigand, J. Rhensius, J. H. Franken, R. Lavrijsen, H. J. M. Swagten, H. Stoll, S. Eisebitt, and M. Kläui, "Magnetic states in low-pinning high-anisotropy material nanostructures suitable for dynamic imaging," Phys. Rev. B **87**, 134422 (2013).

---

1. Introduction

Soft X-ray Fourier transform holography (FTH) is a coherence-based imaging technique that, in contrast to other existing imaging tools, requires neither lenses nor other optical elements for the image acquisition [1]. Instead, the Fraunhofer far field scattering intensity of the sample is recorded, which is given by the amplitude squared of the Fourier transform of the sample transmission function. This transmission function can be digitally reconstructed by an inverse Fourier transform to obtain an image of the object of interest. Such a reconstruction is possible because the required phase information is encoded in the interference pattern between the beam scattered from the sample and an off-axis coherent reference beam from a point-like source [1].

X-ray holography is the only X-ray imaging technique encoding the full complex wave field information. As such, it has a number of advantages: (i) Because no optical elements are required in the focused beam, it is suitable for fully destructive single shot imaging with a very intense photon pulse such as those provided by free electron laser sources [2]. (ii) In such a single shot image, time delays can be encoded, allowing for single shot femtosecond dynamic imaging [3], which is the best temporal resolution reported for the dynamic imaging with sub-50 nm spatial resolution so far. As a further advantage, the imaging acquisition in such a single shot experiment does not require pump-probe reproducibility. (iii) The full wave field information enables post-process refocusing through computational wave field propagation [4], reconstruction of 3D information [5] from a single hologram, and *a posteriori* numerical generation of various contrast mechanisms [6]. (iv) Any drift during the imaging results in a shift in the Fourier space scattering pattern and thus translates into a phase shift in the real space reconstruction. There is no drift of the real space information as long as the internal structure of the object is rigid. It has been demonstrated that this leads to a resolution of better than 3 nm when tracking the center of mass of specific features in a dynamic imaging experiment [7]. (v) The imaging is based purely on photons, and is therefore practically insensitive to electro-magnetic fields in the vicinity of the sample. This, in combination with the large space available around the sample (since no other optical elements are required), makes this technique particularly well suited for sample characterizations in extreme environments, such as simultaneous large magnetic fields and low temperatures [8]. However, despite all these outstanding features, FTH is still not widely used. One of the most significant hindrances is the complexity of the sample fabrication, which we address in this paper.

Despite the critical role played by the sample fabrication for X-ray holography, little details of the fabrication steps have been addressed in a systematic fashion in the literature. Also, a number of approaches such as movable masks [4, 9] and holography with multiple objects holes [10–13] exist, without any reports comparing their performance. Here, we report the details of the fabrication of X-ray holography samples optimized for high performance and suitable for pump-probe magnetic imaging. Major parts of the process are generic and can be adapted for any holographic sample. We show that, to a large extent, both the sample fabrication as well as the image reconstruction are automatable and thus allow for high throughput with minimum human workload.

2. Methods

The nanostructuring of the samples is performed by electron beam lithography (EBL) using a Vistec EBPG 5000 operating at 100 kV acceleration voltage and by focused ion beam (FIB) milling using a dual beam FEI Helios NanoLab 600, which provides a Ga^+ ion beam at variable ion energies of up to 30 keV. Parts of this process have been successfully tested on a widely available Raith e_LiNE and on a Raith PIONEER EBL system, both operated at 20 kV acceleration voltage. Sample characterization is performed using standard scanning electron microscopy (SEM), transmission electron microscopy (TEM), and X-ray holographic imaging at the UE52-SGM beamline of BESSY II (Berlin). The FTH performance test is carried out in the single bunch mode, in which the repetition rate of the incident photon pulses is reduced to 1.25 MHz, making it most interesting for pump-probe dynamic imaging.

3. Sample fabrication steps

X-ray holography samples consist of two parts: (i) a holographic mask with (at least) two apertures (a larger one defining the field of view, and a smaller one, ideally point-like, providing the reference beam), and (ii) the object of interest, which is positioned in close proximity in front or behind the larger aperture. The larger aperture is typically a hole in an opaque film,
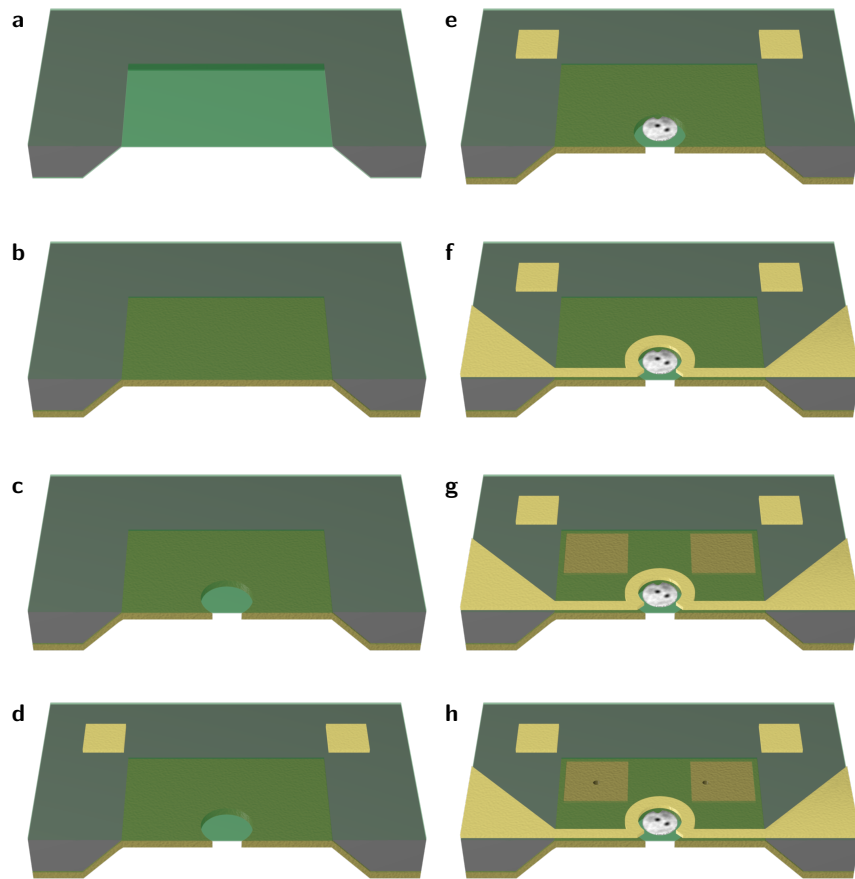
Fig. 1. Sample fabrication steps for pump-probe X-ray holography. (a) Si frame (gray) with Si_3N_4 membrane (transparent green) and extra Si_3N_4 coating on the back side. (b) Deposition of a Cr/Au multilayer on the back of the membrane. (c) FIB milling of an 800 nm diameter object hole in the Cr/Au film. (d) EBL definition of aligned markers on the flat membrane. (e) Preparation of a magnetic specimen (here: a disk) on the top side of the sample, aligned with respect to the center of the object hole (after film deposition, EBL etch mask fabrication, and Ar milling). (f) EBL fabrication of the microcoil around the magnetic disk. (g) Local removal of the Si_3N_4 for the reference milling by FIB. (h) FIB milling of the reference holes in the Cr/Au multilayer.

referred to as the object hole. It is highly beneficial to integrate the object in the holographic mask, to ensure that the mask does not drift with respect to the object. The fabrication steps of such an integrated sample, which we will discuss in detail next, are schematically depicted in Fig. 1, and micrographs of the sample at important steps are presented in Figs. 2–4. Steps 1 (object aperture) and 5 (reference) are generic for all holography samples with an absorption mask (which is required to perform measurements without blocking the direct beam). Steps 2 (alignment) and 3 (specimen) show one possibility of precisely aligning a particular specimen with the field of view, and step 4 (excitation) provides an example of integrating a pump-probe excitation setup in the sample.

3.1. Substrates

The samples presented here are designed for imaging in the extreme ultra-violet to soft X-ray regime, i.e., for energies between 50 eV and 900 eV. The light in this energy range has wide applications in scientific research (i) because the wavelength resolution limit is in the low nanometer regime and (ii) because many important characteristic resonances of different materials in this regime provide access to a large variety of material properties (such as the local magnetization through the X-ray magnetic circular dichroism (XMCD) effect [14]). However, in this energy range, all materials absorb strongly, and therefore the samples have to be sufficiently thin to allow for FTH transmission-based imaging. Widely used substrates are low stress Si_3N_4 membranes, which are commercially available and can be purchased in thicknesses ranging from some ten nanometers up to about one micrometer, with lateral diameters ranging from a few micrometers up to a few millimeters. Here we use 350 nm thick membranes of $10 \times 10 \, \mu m^2$ lateral size on $5 \times 5 \times 0.2 \, mm^3$ Si frames bought from Silson Ltd. [15].

The customized substrates, schematically shown in Fig. 1(a), are prepared by lithographically defining etch mask windows on a Si_3N_4 film deposited on the back of the $Si_3N_4/Si(001)$ samples and etching the Si through the back using a KOH solution to expose the top Si_3N_4 film from the bottom [16]. High-ohmic Si is used to keep the electrical capacitance of the substrate at a minimum and, therefore, to permit high frequency electrical circuits on the samples. Furthermore, of the total 350 nm Si_3N_4, 200 nm are deposited on the Si wafers before the KOH etching, and the remaining 150 nm are deposited on the back side after the etching to provide a good insulation against the sample holder. The thickness of the Si_3N_4 chosen corresponds to a compromise between, on the one hand, good X-ray transmission (thinner membranes) and, on the other hand, mechanical stability, tolerances in the subsequent sputter etch processes, and good electrical insulation with respect to the back side of the membrane at high frequencies (thicker membranes). The lateral dimensions of the membrane were made as small as possible while still compatible with the fabrication process. This enhances the mechanical stability and helps to keep the electrical resistance of impedance-matched transmission lines on the sample low (see section 3.5). The outer dimensions of the Si frame warrant convenient handling of the samples throughout the whole process and, at the same time, provide economic use of the wafer substrates. Membrane substrates such as described here are available in wafers with arrays of up to several hundred single membranes, and all the subsequent fabrication steps are developed such that parallel processing of a whole 4 inch wafer is possible.

3.2. Step 1: Object aperture

To define the object aperture, the Si_3N_4 membrane is first covered from the back side with a thermally evaporated $[Cr(5)/Au(55)]_{20}$ (thicknesses given in nm) multilayer (Fig. 1(b)). This multilayer is fully opaque to the incident X-rays (transmission of less than 10^{-6} for the whole given energy range; the number of repeats can be adapted for applications in a more specific energy range). The periodic interruption of the Au layers by thin Cr layers prevents the formation of large Au grains, which increases the reproducibility of the milling rates in FIB structuring. In this opaque Cr/Au multilayer thin film, a small aperture of about 800 nm diameter is milled by FIB at 8 kV acceleration voltage and 70 pA beam current, stopping at the X-ray transparent Si_3N_4 (Figs. 1(c), 2(a), and 2(b)). The ion dose to stop at the Si_3N_4 is determined by dynamically checking the milling progress using the SEM in the dual beam SEM/FIB. The low energy of the Ga^+ ions reduces sub-surface damage and therefore the annealing of the Au and the formation of hard grains (and, besides, also minimizes sub-surface damage of already deposited specimen on the other side of the membrane due to the reduced ion penetration depth). Hence, the determined milling dose is applicable to all Cr/Au multilayers grown in the same batch, facilitating the automation of the object hole fabrication. For the processing of full waver with
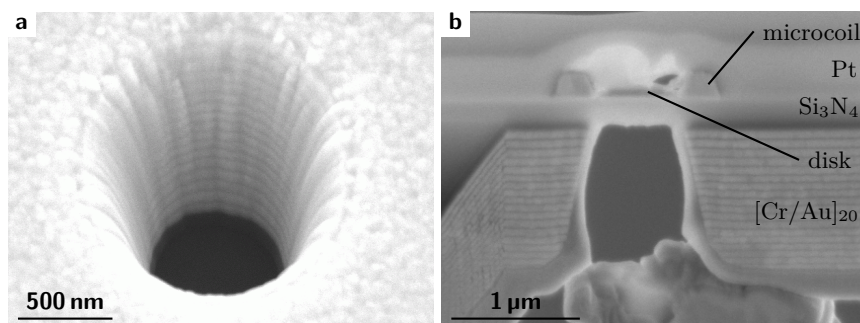
Fig. 2. Scanning electron micrographs of the object hole milled into the Cr/Au layer. (a) View under 30° with respect to the surface normal, showing the Cr/Au multilayer stack (Au appears bright, Cr gray, and Si_3N_4 black). (b) Vertical cross section. The object hole is visible as an horizontal interruption of the periodic Cr/Au multilayers. A dust particle has fallen on the object hole before the preparation of the lamella.

a regular array of membranes, the precision of a standard SEM stage is sufficient to automatically drive to the micrometer-sized membrane without using markers. Focus and stigmator adjustments are not very critical for this process. If required, the Si_3N_4 layer at the object hole can be thinned in this step to improve the aperture transmission. The thinning process can also be done with a high degree of reproducibility.

The round shape of the object hole provides a scattering pattern that is most convenient for the hologram acquisition as well as for the reconstruction process. We find that for aperture diameters smaller than approximately 800 nm, holograms can be recorded without a beamstop for the direct beam, which significantly improves the image quality and enables fully automatic reconstructions, see Sec. 4. Even though multi-object holography has been successfully carried out in the past [10–13], with its well known advantages, such as identical environments for all investigated specimens, we find that the signal from one object is noise for the reconstruction of the other objects and that the highest efficiency is reached when illuminating just one object aperture.

3.3. Step 2: Alignment

After the preparation of the object aperture, Au markers are fabricated on the top side of each substrate at well-defined distances with respect to the object hole using EBL and standard lift-off techniques (Fig. 1(d)). Note that ultrasound (for instance for aiding the resist development and the lift-off process) cannot be used at any time as this would rupture the membrane. The alignment is achieved by first preparing dummy markers optically aligned with the membrane, and then measuring the coordinates of the object hole with respect to these markers using a pattern-recognition algorithm to automatically find the object holes (which appear as dark circles with characteristic diameter in the SEM images, see Fig. 3(a)). With the Vistec system, the alignment is reproducible and accurate to better than 20 nm despite the insulating substrates. However, it is important to keep the electron intensity at a minimum, e.g., by using a small beam current and by sufficient breaks between exposure steps. At lower electron energies, where charging becomes more problematic, ESPACER™300 conducting resist (by Showa Denko K. K. [17]) has proven successful in reducing charging.
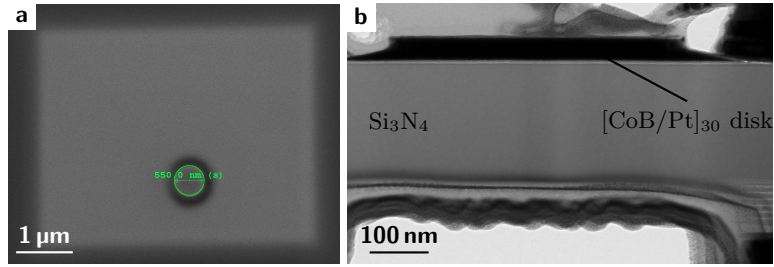
Fig. 3. Magnetic disk. (a) SEM view of the top side of the Si$_3$N$_4$ membrane. The membrane is visible as a bright rectangle due to electron backscattering from the Au layer underneath. The object hole is visible as a dark circle around the magnetic disk. (b) TEM image of a vertical cross section, which is a zoom-in of the area shown in Fig. 2(b).

3.4. Step 3: Specimen

As an example, we discuss the fabrication process for samples used in the investigation of magnetic field-induced dynamics of magnetic domains [7]. The magnetic specimen is a disk-shaped element with an artificial notch that is designed to act as a nucleation center in the dynamic excitation process. The disk is smaller than the field-of-view provided by the object aperture to ensure that the dynamics of the whole element is captured (Figs. 1(e), 3(a), and 3(b)). The disk is fabricated (i) by sputtering a continuous magnetic film on the flat side of the holography substrates, (ii) negative-tone EBL to produce a disk-shaped etch mask, and (iii) a subsequent neutralized Ar atom sputter-removal of the material everywhere apart from the disk. We use hydrogen silsesquioxane (HSQ) resist, enabling nanometer-resolution lithography and providing a sufficiently robust etch mask of SiO$_2$, which is transparent to soft X-rays and does not need to be removed for imaging. It is important to protect the alignment markers throughout these steps to allow for their automatic recognition. The means of marker protection must be adapted to the specifications of the lithography system that is employed in the succeeding steps: When using a Vistec machine, the distance of the alignment markers to the area of exposure is not critical for the alignment precision, and markers can be placed at the edge of the sample. In contrast, with the Raith systems, the alignment precision is significantly enhanced when the markers are present in the write field area, i.e., when the stage does not move after the marker detection. For this reason, we use a coarse mask, such as Kapton, to protect the markers from metal deposition when further patterning is performed with the Vistec machine, whereas lithographic lift-off masks are required when using the Raith systems. To protect the markers during the Ar milling, we expose the HSQ on top of the markers in all cases.

3.5. Step 4: Excitation

The next step is to prepare a microcoil for magnetic excitations wound tightly around the disk (Figs. 1(f) and 4). We use a Au wire with a cross section of $300 \times 300\,\text{nm}^2$, which results in a $50\,\Omega$ impedance against the Au ground on the back side of the membrane, as required for GHz microwave transmission. The wire dimensions take into account the thickness of the Si$_3$N$_4$. Outside the membrane area, the wire width is increased according to the local thickness of the Si wafer (which has a constant slope in the region that defines the membrane window), up to a width of $170\,\mu\text{m}$ on the bulk substrate. This ensures the $50\,\Omega$ impedance matching of the whole microstrip.

The microcoil is fabricated in a lift-off process, where we use $1\,\mu\text{m}$ thick polymethyl-methacrylate (PMMA) resist exposed via EBL with electron energies of $100\,\text{keV}$, and a $7:3$
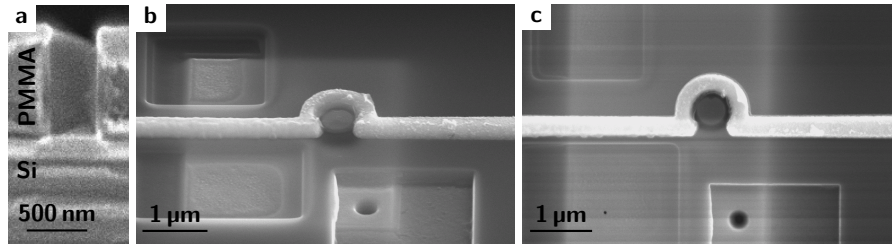
Fig. 4. SEM images of the final fabrication steps. (a) Cross section through a 330 nm wide line defining a mask in 750 nm thick PMMA for the Au microcoil deposition. The variation of the width of the line as a function of vertical position is negligible, i.e., the PMMA walls have no undercut. (b) Image of the final sample before preparation of the second reference. The sample is tilted by 52° with respect to the incident electron beam. The image shows the magnetic disk in the center, which is tightly surrounded by a Au microcoil. In this particular sample, three areas of Si_3N_4 are removed to prepare the references where one reference has already been prepared with the cone on the top side (the side from which the image was taken). (c) Top-view of the same sample after the preparation of another reference from the bottom side.

mixture of isopropanol and water for the development [18], to achieve steep side walls in the resist (i.e., to avoid undercut), as shown in Fig. 4(a). With such steep side walls, the position and the width of the microcoil are precisely defined and the coil can be prepared in close proximity to the magnetic disk, see Figs. 4(b) and 4(c). We note that a pre-exposure bake of the PMMA for 60 s at 120 °C proved sufficient for our lithography, which is important for specimens that cannot withstand high temperatures.

The exposure runs automatically by using the previously protected markers for the alignment. At low electron energies, optimal alignment precision requires the removal of the PMMA layer around the markers by electron exposure and development before the actual exposure of the microcoil. Furthermore, the inevitable undercut in the PMMA mask that is characteristic for low electron energies has to be considered in the exposure layout. Our specific microcoil has an inner diameter of 760 nm. It has been shown that this coil geometry is suitable to generate field pulses with approximately 100 ps rise time and 40 mT peak strength at the coil center [7].

3.6. Step 5: Reference holes

The reference holes are narrow cylinders milled through the entire material stack of Si_3N_4 and Cr/Au (note that other reference aperture geometries, such as edges [19], have been demonstrated as well, but the resolution is always limited by the smallest feature size of the FIB). The Si_3N_4 is removed with the FIB around each reference hole before milling to avoid problems when the ion beam hits the interface between (hard) Si_3N_4 and (soft) Au (Figs. 1(g) and 4). The reference holes are then milled with a 30 keV Ga^+ ion beam at 30 pA beam current focused to a spot size better than 20 % of the target reference hole diameter (practical value). In a first step, the Cr/Au is removed in a 500 nm wide and roughly 500 nm deep cone, and afterwards, a circular hole of the desired diameter (50 nm in our application, corresponding to a reference-limited resolution of approximately 35 nm [20]) is milled through the remaining Cr/Au layers (Figs. 1(h) and 4). The usage of the highest ion energy leads to the best contrast in images taken with the ion beam, and thus allows for optimal beam adjustment and provides the smallest spot size. The cone reduces the aspect ratio of the reference tube, and allows for the sputter-removed material to leave the hole. Still, the high aspect ratio of the reference holes hinders the fabrication of holes with diameters near the spot size of the ion beam. In contrast to all other fabrication

steps, the fabrication of high-quality reference holes could not be fully automated with the FIB used here because it requires a manual beam adjustment for each membrane sample.

4. Performance

Samples prepared according to the recipe presented before have successfully been used in a pump-probe dynamic imaging experiment published elsewhere [7]. Here, we discuss the efficiency of the design determined from these measurements. We obtain images of the magnetic state of our disk by X-ray holographic imaging using holograms taken with positive and with negative helicity photons at the Co L_3 absorption edge (778 eV), as described in Ref. [1]. Our specific magnetic material is a Pt(2)/[Co$_{68}$B$_{32}$(0.4)/Pt(0.7)]$_{30}$/Pt(1.3) (thickness in nm) multilayer stack, which is optimized for pump-probe dynamic imaging [21], in particular for Skyrmion dynamics [7]. An image of the magnetization component projected onto the photon propagation direction is reconstructed by an inverse Fourier transform of the difference of the holograms taken with positive and with negative helicity, utilizing the fact that this difference contains only the magnetic information due to the XMCD at the given photon energy. Here, our sample is mounted perpendicular to the incident beam, and we are sensitive to the thickness-integrated out-of-plane component of the magnetization. Holograms are acquired using a Princeton Instruments PI-MTE CCD camera with 2048×2048 pixel, each $(13.5 \, \mu m)^2$ in size, operated at 1 MHz readout speed. The camera is placed 293 mm downstream of the sample, resulting in a maximum recordable wave vector transfer of $q_{max} = 0.34 \, nm^{-1}$ at an incident wave length of $\lambda = 1.59 \, nm$. The associated resolution limit of the numerical aperture is 34 nm, which has been designed to match the resolution limit of the reference.

The image reconstruction works reliably with a fully automatic script. This is possible because our design allows for the imaging without beamstop and therefore for an accurate automatic determination of the center of the image required by the Fourier transform. This automatic centering has not been reported for any other holographic sample design so far. Our script finds the center of the hologram with sub-pixel precision by searching for the maximum of the total number of counts in a circle with a 10 pixel radius and variable origin in a 20×20 pixel area around the brightest pixel in the sum of all holograms. Furthermore, before the Fourier transform, two algorithms are applied to the difference hologram to improve the quality of the reconstructed image: (i) filtering of parasitic signals such as cosmic rays and dead pixels identified by their intensity deviating by more than 6 standard deviations from the average local intensity in a 32×32 pixel environment, and (ii) zero padding of the hologram to double its original size. The magnetic disk is a small area in the transformed hologram, which is cropped using the topography image obtained by reconstructing the sum holograms from both helicities, see Fig. 5(a). Finally, the complex phase is optimized for maximum contrast (variance) in the real part of the image. This real part yields the images of the magnetic domains (Figs. 5(b) and 5(c)), in our case showing that the magnetization is pointing predominantly downwards, apart from two circular areas, so-called bubble domains. The radius of these bubbles is approximately 50 nm. The images shown in Figs. 5(b) and 5(c) are reconstructed from holograms taken with distinct integration times. We find that a total number of 6×10^7 detected photons per helicity is required to obtain an image of the magnetic state, see Fig. 5(b). These photons are inhomogeneously distributed across the camera chip, with the distribution being characteristic for the specimen and the mask geometry. With our particular mask design, the total number of 6×10^7 photons corresponds to 2300 photons (1.5×10^5 camera counts) in the brightest pixel. Because the sensitivity of our camera becomes non-linear if more than 3.5×10^4 counts are recorded
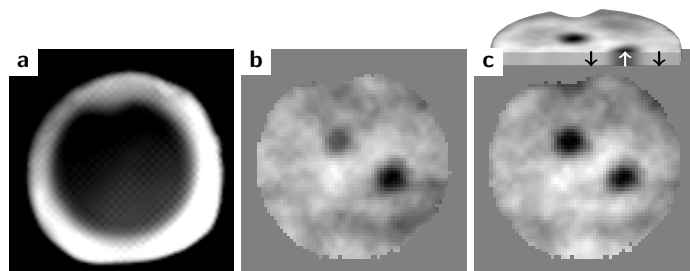
Fig. 5. Holographic reconstructions of a magnetic state obtained with the presented sample design. (a) Topography of the specimen, which is a 550 nm diameter disk with a notch at the top centered to the 800 nm diameter field of view defined by the object hole (white circle). (b) Reconstruction of the magnetic state from a difference hologram with 6×10^7 photons per helicity, cropped to the disk area. The magnetization is pointing downwards (away from the reader) in the white regions, whereas it is pointing upwards in the black areas. The image shows a magnetic configuration with two bubble domains. (c) Reconstruction of the same state from 1.3×10^7 photons per helicity. The orientation of the magnetic domains is depicted on top on the image in a schematic cross section through the disk.

in a single pixel, 4 camera readouts per helicity are required to obtain an image of the quality shown in Fig. 5(b). The total acquisition time of a single image with our sample design and the presently available photon flux is less than 2 minutes plus the additional time for changing the helicity.

5. Conclusions

In conclusion, we presented a fabrication scheme for samples apt for pump-probe soft X-ray Fourier transform holography. The design has been optimized to acquire high resolution (sub-40 nm), high quality images in the low flux single bunch mode in a few minutes. With this acquisition speed, movies of magnetic dynamics with a sufficiently large number of frames can be recorded. Apart from the milling of the reference holes, which requires manual focus-tuning for every membrane, all fabrication steps can be automated. Hence, the process can be used in mass-production. Furthermore, our particular design facilitates the fully automatic reconstruction of the holograms, providing real-time access to the image information. We expect that our scheme will make time-resolved X-ray holographic imaging more accessible to the larger scientific community.